





Article

Modelling, Design, and Control of a Central Motor Driving Reconfigurable Quadcopter

Zhuhuan Wu, Ke Huang and Jiaying Zhang

Topic

Innovation and Inventions in Aerospace and UAV Applications

Edited by

Dr. Andrzej Łukaszewicz, Prof. Dr. Mohamed Thariq Hameed Sultan, Dr. Quang Ha,

Dr. Wojciech Giernacki, Dr. Leszek Ambroziak, Dr. Wojciech Tarasiuk and Dr. Andriy Holovatyy









Article

Modelling, Design, and Control of a Central Motor Driving Reconfigurable Quadcopter

Zhuhuan Wu D, Ke Huang D and Jiaying Zhang *D

School of Aeronautic Science and Engineering, Beihang University, Beijing 100191, China * Correspondence: jiaying.zhang@buaa.edu.cn

Abstract

Constrained by fixed frame dimensions, conventional drones usually demonstrate insufficient capabilities to accommodate complex environments. However, the reconfigurable drone can address this limitation through its deformable frame equipped with actuators or passive interaction mechanisms. Nevertheless, these additional components may introduce an excessive weight burden, which conflicts with the lightweight objective in aircraft design. In this work, we propose a novel reconfigurable quadrotor inspired by the swimming morphology of jellyfish, with only one actuator placed at the centre of the frame to achieve significant morphological reconfiguration. In the design of the morphing mechanism, three telescopic sleeves are driven by the actuator, enabling arms' rotation to achieve a maximum projected area reduction of 55%. The nested design of sleeves ensures a sufficient morphing range while maintaining structural compactness in the fully deployed mode. Furthermore, key structural dimensions are optimized, reducing the central motor load by up to 65% across configurations. After deriving parameter variations during morphing, Proportion-Integration-Differentiation (PID) controllers are implemented and flight simulations are conducted in MATLAB. Results confirm the drone's sustained controllability during and after reconfiguration, with an "8"-shaped trajectory tracking root mean square error (RMSE) of 0.109 m and successful traversal through long narrow slits, reducing mission duration under certain conditions.

Keywords: quadcopter; reconfiguration; mechanics; design and control



Academic Editors: Pablo Rodríguez-Gonzálvez, Andrzej Łukaszewicz, Mohamed Thariq Hameed Sultan, Quang Ha, Wojciech Giernacki, Leszek Ambroziak, Wojciech Tarasiuk and Andriy Holovatyy

Received: 7 October 2025 Revised: 17 October 2025 Accepted: 20 October 2025 Published: 23 October 2025

Citation: Wu, Z.; Huang, K.; Zhang, J. Modelling, Design, and Control of a Central Motor Driving Reconfigurable Quadcopter. *Drones* **2025**, *9*, 736. https://doi.org/10.3390/drones9110736

Copyright: © 2025 by the authors. Licensee MDPI, Basel, Switzerland. This article is an open access article distributed under the terms and conditions of the Creative Commons Attribution (CC BY) license (https://creativecommons.org/licenses/by/4.0/).

1. Introduction

As a subset of Unmanned Aerial Vehicles (UAVs), multicopters have exhibited remarkable capabilities to handle missions, including supply delivery, battlefield surveillance, geospatial exploration, as well as search and rescue, owing to their high maneuverability and modular design advantages [1–4]. Due to the proliferating diversity of application scenarios, together with the environmental susceptibility of drones, real-time adaptation and stable operation are becoming new requirements for multicopters working in complex environments to ensure qualified flight performance. But conventional multicopters have inherently limited environmental adaptability for their predefined structural configurations. This constraint further induces a dilemma in working environments, including confined spaces, whether choosing a small drone with poor load capacity and disturbance resistance or selecting a large one with escalated control difficulty and failure probability [5].

Therefore, great attention has been drawn to design multicopters capable of adjusting frames according to different flying conditions, while still taking maneuverability and load capacity into account [6,7]. In recent years, various types of multicopters with morphable

Drones 2025, 9, 736 2 of 22

frames were designed, aiming to transcend the limitation of fixed structures of conventional drones, which can be classified into three categories: tiltrotors, multimodal multicopters, and foldable drones [8].

The underactuated problem limits the flight performance and environmental adaptability of conventional drones in confined spaces, prompting the development of tiltrotors as a solution. By rotating propellers, tiltrotors adjust the direction of net thrust vector and enable multidirectional propulsion. Mounting actuators at the end of arms to tilt propellers, Ryll et al. [9] designed a quadcopter with high maneuverability and demonstrated its superiority under operational regimes unattainable by standard drones, like controlled attitude trajectory tracking. For further realizing omnidirectional control, Kamel et al. [10] adopted a hexacopter platform with fully controlled omnidirectional propellers. This approach decoupled attitude and position control, thus simplifying control allocation and enhancing flight efficiency. While direct actuator integration in the above designs is straightforward, it inevitably increases the overall weight. Additionally, during maneuvers, different orientations between motors induce opposing force components, resulting in degraded operational efficiency. To address these limitations, Zheng et al. [11] developed a fully actuated tiltrotor incorporating a biaxial rotor tilting mechanism. Employing two orthogonally arranged servomotors to actuate a parallel mechanism, the design ensures propellers' parallelism under attainable tilt angles, thus streamlining control strategies while eliminating power dissipation caused by non-parallel thrust vectors. Flight tests further demonstrate that the fully actuated motion reduces the amplitude of roll and pitch oscillations by up to 75% during aggressive maneuvers, compared to the conventional underactuated mode. Lv et al. [12] designed a coaxial tiltrotor employing two pairs of tiltable coaxial motors and a rear thruster. The platform utilizes an adaptive controller for velocity and attitude tracking. Subsequent work introduced a multivariable cascaded finite-time controller with nonlinear control allocation, which achieved a 28% reduction in velocity root mean square error compared to the earlier adaptive controller during flight tests [13].

Multimodal drones utilize the switching of configurations to achieve cross-domain locomotion between ground-air or water-air environments. Meiri et al. [14] developed a hybrid quadcopter called FSTAR, which employed a servomotor to rotate the arms, enabling the transition between crawling mode, when arms are tilted, and flying mode, when extended. It adopts a crawling mode for traversing when encountering constrained spaces such as pipes and gaps, while transitioning to flying mode to fly over large obstacles impossible to climb over. Mishra et al. [15] proposed an aerial-ground bimodal quadcopter with deflectors mounted under the centre of each propeller. In the ground mode, the downwash airflow driven by propellers is redirected by tilted deflectors, propelling the drone to a designated location for object retrieval. Yang et al. [16] presented SytaB, a novel hybrid terrestrial-aerial vehicle where a bicopter is integrated with two passive spherical wheels. The design enables efficient ground locomotion via direct thrust vectoring and ensures smooth aerial-terrestrial transitions through a dedicated transitional mode. Drawing inspiration from the propulsion framework of submersible remotely operated vehicles, Tan et al. [17] designed an aerial-aquatic quadrotor utilizing tiltable propellers. Its singledegree-of-freedom reconfigurable mechanism exploits structural symmetry, employing a single servomotor coupled with a bevel gear transmission to reversely tilt opposite motors. This enables the drone to switch between two modes for underwater propulsion or aerial flight with a simple structure, low weight, and ease of control.

Foldable drones change their dimensions by structural reconfiguration to achieve confined space traversal and agile maneuvers. It mainly comprises two approaches. In the first approach, the drone reconfigures by actively driving specific mechanisms using

Drones 2025, 9, 736 3 of 22

additional installed actuators. Inspired by the origami mechanism, Yang et al. [18] replaced conventional rigid arms with laminate structures, thus effectively adding elastic hinges to the drone's structure. When the servomotor installed at the centre of the drone rotates, it pulls the strings connected to the motor block. The resultant force deforms the laminate structure, facilitating the inward movement of rotors and propellers to reconfigure the quadcopter. Some researchers, however, further increased the degrees of freedom of the folding mechanism to create multiple configurations on a single multicopter platform. Therefore, when encountering various kinds of environments, the drone can switch to an appropriate configuration to sustain acceptable performance. For example, Falanga et al. [19] added servomotors between each of the arms and the main body, enabling the independent control of four arms. The design allows the drone to flexibly adjust its configuration to fly through lateral or vertical gaps, and a configuration-based control algorithm is adopted to achieve flexible real-time control. Whereas in the second approach, the drone passively morphs, relying on the potential energy stored inside or interactions with the environments outside, without adding more actuators. One application of this idea is the collision-resilient drone, whose frame can deform to absorb energy during the collision and recover after the impact, protecting core components stored inside. Inspired by the dual stiffness of insect wings, Mintchev et al. [20] designed a collision-resilient quadcopter by connecting a flexible frame to a central block using magnetic joints. During flight, the block geometrically constrains the frame, maintaining the drone's rigidity, while upon collision, two parts are separated by external forces, allowing the frame to deform freely to absorb the impact energy and protect the components inside the block. Passive reconfiguration is also applied to the deployment of multicopters. Pastor et al. [21] developed an egg-shaped drone that can be launched to deploy, with torsion springs installed at hinges connecting the main body and arms. Before launch, the arms are constrained by a monofilament line to keep the drone's ballistic shape and the springs' compressed state. Once launched, the line is instantly heated and burned, allowing the springs to push the arms for deployment. For clarity, the relevant surveys are summarized in Table 1, including their categories, methods, strengths, and limitations. Despite these differences, minimizing the number of actuators while achieving controlled flight remains one of the most significant objectives across all categories of reconfigurable multicopters.

Table 1. Summary of surveys.

Category	Survey	Methods	Strengths	Limitations	
Tiltrotor	Ryll et al. [9]	Mounting actuators at the end of quadcopter arms to tilt propellers.	Possible to obtain full controllability over the 6-DoF body pose in space.	Do not offer omnidirectional flight capabilities; weight penalty; different orientations between motors degrading efficiency.	
	Kamel et al. [10]	Mounting actuators at the end of hexacopter arms to tilt propellers.	Decoupled position and orientation control; omnidirectional maneuverability.	Weight penalty; different orientations between motors degrade efficiency.	
	Zheng et al. [11]	Employing two orthogonally arranged servomotors to actuate a biaxial rotor tilting mechanism.	Fully actuated, resulting in simplified control strategies; eliminating power dissipation caused by non-parallel thrust vectors.	Mechanism weight penalty (34% of total weight); reduced system reliability due to complex mechanism.	
	Lv et al. [12,13]	Employing two pairs of front coaxial tiltable motors driven by servo motors.	Compact structure; no need to consider reaction torques; possessing control redundancy.	Different orientations between motors degrade efficiency; potential aerodynamic interference between coaxial motors.	

Drones 2025, 9, 736 4 of 22

Table 1. Cont.

Category Survey		Methods	Strengths	Limitations
Multimodal drone	Meiri et al. [14]	Employing a servomotor to rotate the arms.	Capable of fly and sprawl to adapt complex working environments; exploiting ground mode to save energy.	Always spinning wheels in flight due to fixed propeller–wheel coupling; weight penalty.
	Mishra et al. [15]	Mounting deflectors under the centre of each propeller to deflect airflow for the ground locomotion.	Robust to the effect of ground wash in grasping tasks; potential to extend to water navigation.	Lack of steering capability; weight penalty due to reflectors and driving actuators.
	Yang et al. [16]	Designing a bicopter integrated with two passive spherical wheels.	Directly producing the heading thrust; smooth transition between modes.	Limited payload capacity due to bicopter configuration; limited lateral movement.
	Tan et al. [17]	Employing a single servomotor coupled with a bevel gear transmission to reverse the tilt of opposite motors.	Single propulsion system for both mediums; thrust vectoring capability; mechanically simple symmetric design.	Power inefficiency due to constant thrust for submergence; limited payload capacity.
Foldable drone	Yang et al. [18]	Central motor rotation to pull elastic laminate arms or release.	Lightweight structure; low-cost cardboard fabrication; adaptability to cluttered environments.	Limited structural durability of cardboard laminate; limited payload capacity due to lightweight materials.
	Falanga et al. [19]	Adding servomotors between each of the arms and the main body.	Capability of transforming into multiple configurations to adapt to different environments; employing adaptive control for various task stability.	Weight penalty due to servomotors, resulting in limited payload capacity; reduction in flight time in non-X configurations.
	Mintchev et al. [20]	Connecting a flexible frame to a central block using magnetic joints.	Collision-resilient to protect core components hosted in the central case of the drone.	Limited payload capacity; limited protection in upside-down crashes.
	Pastor et al. [21]	Burning the constraining monofilament line to allow springs to push the arms for deployment.	Rapid deployment by launching; flexible launching conditions, including moving platforms.	Single-use burn-wire mechanism requires manual reset; limited propeller size due to barrel diameter constraint.

Considering the demand of traversing confined environments and the pursuit of light weight, this paper presents a novel reconfigurable quadcopter design based on a central-motor-driving telescopic mechanism, conceptually inspired by the radial symmetry and significant contraction of the jellyfish's morphology during the swimming process, as demonstrated in Figure 1. By simulating the jellyfish's bell through four arms and integrating the function of the jellyfish's specialized muscles into a telescopic mechanism along the drone's central axis, the proposed solution achieves the drone's configuration changes through the inward folding and outward deployment of the arms, which effectively changes the lateral span of the drone. The resultant maximum shrinkage rate in the area projected onto the chassis plane is measured to be 55%. This enables the drone to navigate obstacles in confined conditions, thus enhancing the drone's maneuverability and adaptability to complex working environments. In addition, since only one actuator is added for reconfiguration, the design balances the reconfigurability and weight penalty. Additionally, due to the usage of thread engagement in the telescopic mechanism, continuous angle change between the arms and the drone's central axis is achieved, allowing it to

Drones 2025, 9, 736 5 of 22

morph and fly at any angle within the designed operational range. Finally, the Proportional–Integral–Differential (PID) control method is employed to enable stable control of our drone both during and after the reconfiguration process. This paper primarily contributes to the foundational stage of this novel design by encompassing the conceptual design, kinematic and dynamic modelling, parameters optimization, and control strategy. The scope of this work is thus focused on validating the functional feasibility and controllability of the morphing concept at the system dynamics level, with numerical simulations concentrating on trajectory tracking and gap-traversal performance to establish a theoretical groundwork for future experimental implementation.

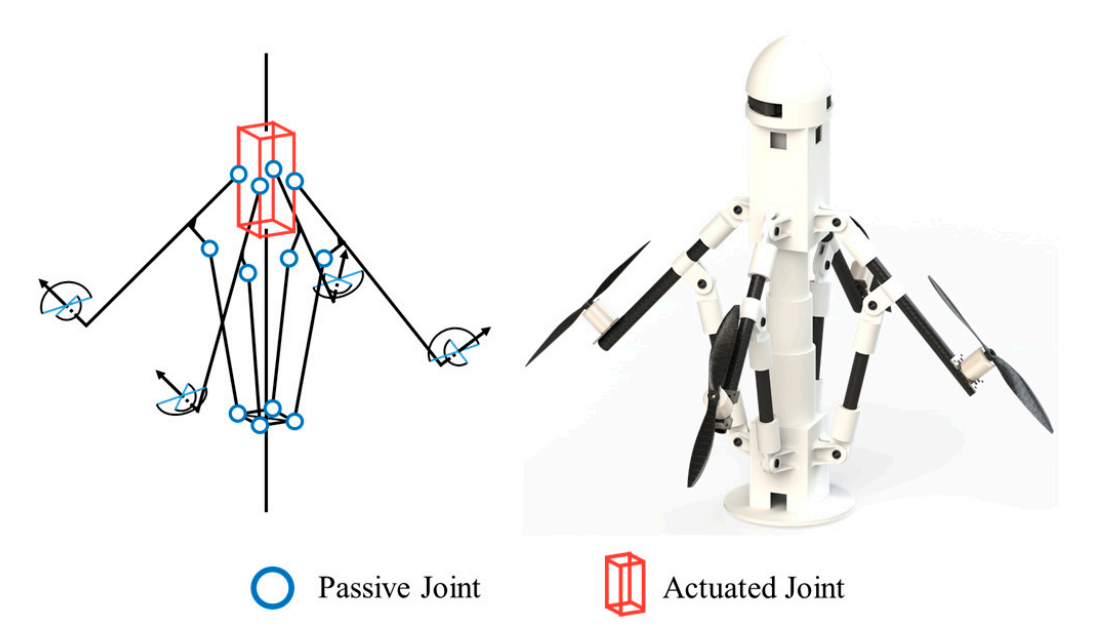


Figure 1. Novel reconfigurable drone (right) and kinematic design (left).

The contributions of this article can be summarized as follows:

- We present a novel reconfigurable quadcopter that achieves a significant 55% reduction in the projected area with only one central motor, which effectively balances morphing capability with light weight.
- We conduct a dimensional optimization of the mechanism that significantly minimizes the axial load on the central motor, enhancing its reliability and efficiency.
- We demonstrate that continuous and stable morphing flight is achievable, as validated by numerical simulations employing a PID control strategy.

This paper is organized as follows. Section 2 introduces the design overview of this novel reconfigurable quadcopter, and the kinematic and dynamic characteristics of the drone are further derived to obtain quantified parameter variations during the reconfiguration process. Section 3 presents the control strategy of the drone, and Section 4 concludes the paper. For clarity, the definitions of the key symbols used throughout this work are organized in Table 2.

Drones 2025, 9, 736 6 of 22

Table 2. Definitions of the key symbols.

Distance between the connector and the main body	s_2	Distance between main body hinges
Support rod length	s_4	Connector length
Arm length	ζ	Reconfiguration angle
Central sleeves telescoping velocity	$\omega_{ m arm}$	Rotational angular velocity of arms
Hight of central gravity	H_{CL}	Height of centre of lift
Mass moment of inertia matrix	v	Velocity vector in body frame
Position vector in inertial frame	ω	Angular velocity vector in body frame
Euler angle vector	F	Thrust force vector
Thrust moment vector	$R^{ m BE}$	Rotational matrix from inertial frame to body frame
Gravity vector in inertial frame	Н	Transformation matrix from body angular velocity to Euler angle angular velocity
Commanded acceleration vector	$v_{ m cw}$	Constant wind velocity
Sinusoidal gust velocity	RMSE	Root mean square error
Mean square error	IAE	Integral absolute error
Integral squared error	ITAE	Integral time absolute error
	connector and the main body Support rod length Arm length Central sleeves telescoping velocity Hight of central gravity Mass moment of inertia matrix Position vector in inertial frame Euler angle vector Thrust moment vector Gravity vector in inertial frame Commanded acceleration vector Sinusoidal gust velocity Mean square error	connector and the main body s_2 Support rod length s_4 Arm length ζ Central sleeves telescoping velocity ω_{arm} Hight of central gravity H_{CL} Mass moment of inertia matrix v Position vector in inertial frame ω Euler angle vector F Thrust moment vector R^{BE} Gravity vector in inertial frame H Commanded acceleration vector v_{cw} Sinusoidal gust velocity $RMSE$ Mean square error IAE

2. Modelling and Parameter Optimization

2.1. Design Overview

The design of our reconfigurable drone is based on the mature quadcopter platform, whose inherent symmetry naturally aligns with the symmetrical morphology of jellyfish. To further simulate the specific muscles responsible for bell contraction of jellyfish, a servomotor is mounted at the bottom motor base of the quadcopter, driving a telescopic mechanism to rotate the arms, thereby achieving reconfiguration of the drone.

The structure of our reconfigurable drone is shown in Figure 2, which mainly consists of an integrated power module, a battery storehouse, four arms, support rods, motors, and propellers, as well as the telescopic mechanism for the drone's reconfiguration. A flight controller is placed on top of the integrated power module. The module further interconnects with the battery storehouse via snap fittings, which are hinged to the arms. The telescopic mechanism is mounted below the storehouse and connects to the support rods through hinges. As the arms finally connect with the support rods, a four-bar mechanism is formed, enabling the drone to contract or deploy the arms under the central motor's actuation. When encountering narrow environments that require traversal, the telescopic mechanism extends, folding the arms towards the main body, thus reducing the effective span for traversal. During normal flight, the telescopic mechanism keeps its shortest length, with the arms perpendicular to the drone's central axis. In this configuration, the maximum lift is realized for the full usage of propeller thrust, ensuring efficient flight of the drone.

Drones 2025, 9, 736 7 of 22

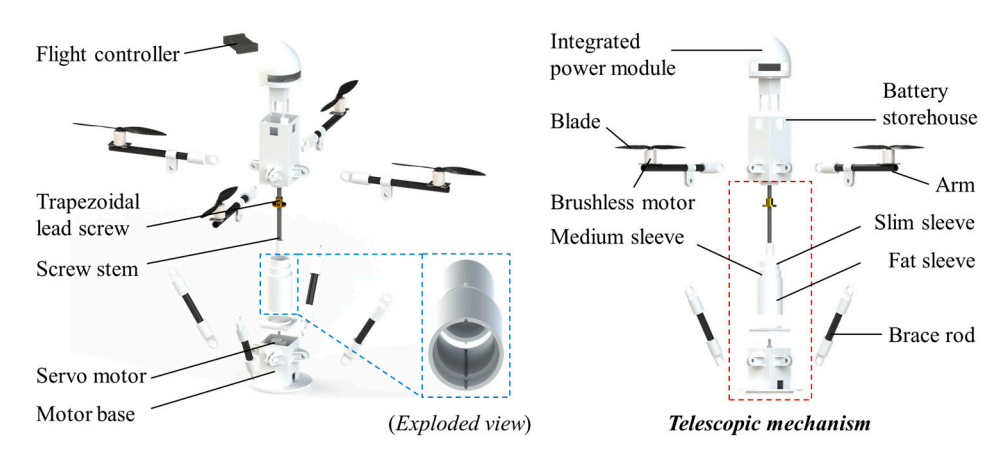


Figure 2. Exploded view of the prototype design rendered in CAD.

The telescopic mechanism comprises a slim sleeve, medium sleeve, fat sleeve, screw stem, trapezoidal lead screw, motor base, and servomotor. The three sleeves are designed to fit sequentially with minimal clearance, ensuring both smooth sliding and full storage. In addition to the mechanism's large adjustable range, the design also guarantees low resistance and energy consumption during the reconfiguration process. Additionally, a protrusion-slot design is adopted to connect adjacent sleeves, to constrain the rotational degree of freedom and the extreme position of sliding. The trapezoidal lead screw is fixed on top of the slim sleeve and engages with the screw stem, which is connected to the servomotor via coupling. When the motor rotates, the screw stem converts the rotational motion into linear motion of the trapezoidal lead screw, further extending or retracting the sleeves for arms' rotation. To precisely define the prototype, the key dimensions of these main components are summarized in Table 3. It should be noted that the final dimension of the support rod, which is determined through a subsequent optimization process to minimize the central motor load, is also included for completeness and will be discussed in detail in Section 2.2.

Table 3. Dimensions of the main components.

Component	Dimensions		
Blade (APC 1047)	Diameter: 10 in (\approx 254 mm).		
Battery storehouse	$70~\text{mm} \times 70~\text{mm} \times 150~\text{mm}$; thickness: 2 mm.		
Slim sleeve	External diameter: 46 mm; height: 80 mm; thickness: 3.5 mm.		
Medium sleeve	External diameter: 53 mm; height: 80 mm; thickness: 3.5 mm.		
Fat sleeve	External diameter: 60 mm; height: 85 mm; thickness: 3.5 mm.		
Motor base	$70 \text{ mm} \times 70 \text{ mm} \times 95 \text{ mm}$; thickness: 2 mm.		
Arm	Length: 250 mm.		
Brace rod	Length: 180 mm.		

2.2. Folding and Deploying Mechanism of Reconfigurable Drone

2.2.1. Mechanics of Reconfiguration Mechanism

The kinematic relationship of the reconfiguration mechanism lays the foundation for designing the reconfigurable quadcopter. To obtain the relationship between the length of the central sleeves and the arms' rotation angle, the arm, support rod, and telescopic mechanism are simplified into a crank-slider mechanism, as shown in Figure 3a. Points

Drones 2025, 9, 736 8 of 22

A, B, and N represent hinges, while AM and BN represent the arm and support rod, respectively. To accurately rebuild the actual model, the size of the connector is considered by introducing the DN segment. Assume $\|AD\| = s_1$, $\|AB\| = s_2$, $\|BN\| = s_3$, $\|DN\| = s_4$, and the length of the arm $\|AM\| = L$, which means that $\|DM\| = L - s_1$. To avoid the occurrence of dead point, the sizes should satisfy $s_3 > \sqrt{s_1^2 + s_4^2}$.

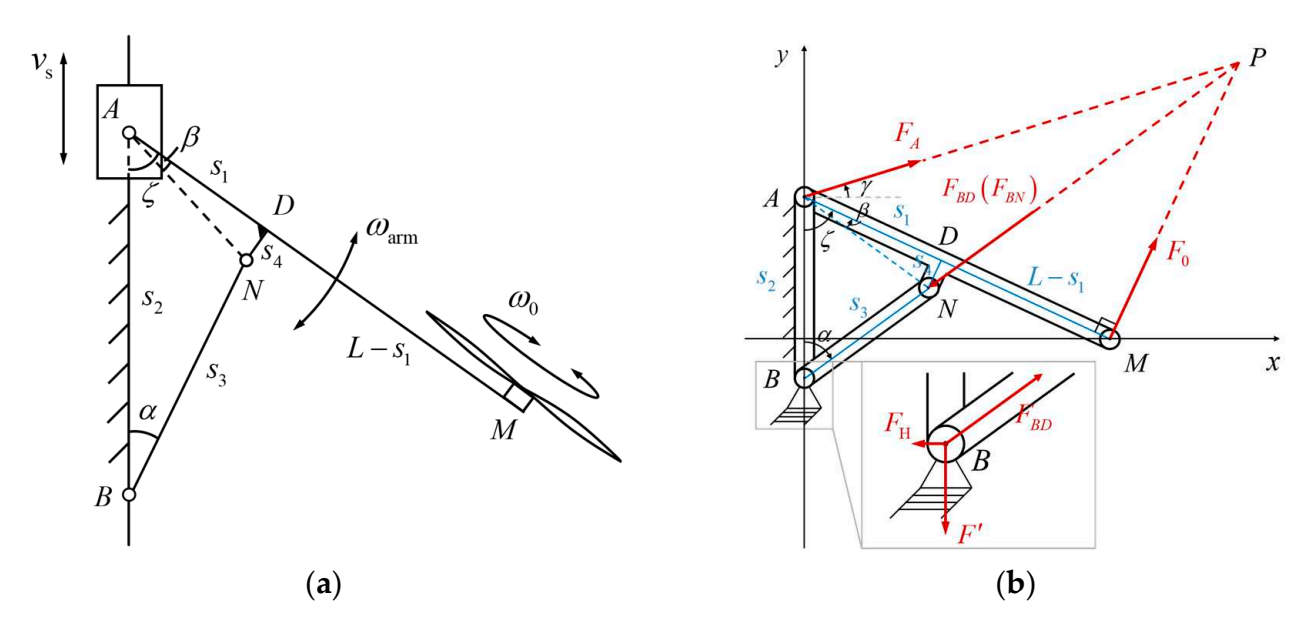


Figure 3. Equivalent structural modelling: (a) the crank-slider mechanism and (b) the force diagram.

Assume the reconfiguration angles $\angle BAM = \zeta$, $\angle ABN = \alpha$, $\angle DAN = \beta$. From the law of cosines, the varying length s_2 and angle α can be expressed as

$$s_2 = \sqrt{s_1^2 + s_4^2} \cos(\zeta - \beta) + \sqrt{s_3^2 - (s_1^2 + s_4^2) \sin^2(\zeta - \beta)}$$
 (1)

$$\alpha = \cos^{-1} \frac{s_2^2 + s_3^2 - s_1^2 - s_4^2}{2s_2s_3} \tag{2}$$

During the reconfiguration process, the telescoping velocity v_s is related to s_2 as

$$v_{\rm s} = \frac{\mathrm{d}s_2}{\mathrm{d}t} \tag{3}$$

Therefore, the rotational angular velocity ω_{arm} of the arm can be expressed using velocity v_s and the results in (1) as

$$\omega_{\text{arm}} = \frac{\mathrm{d}\zeta}{\mathrm{d}t} = \frac{\mathrm{d}(\zeta - \beta)}{\mathrm{d}s_2} \frac{\mathrm{d}s_2}{\mathrm{d}t} = -\frac{1}{\sqrt{1 - \left(\frac{s_1^2 + s_4^2 + s_2^2 - s_3^2}{2\sqrt{s_1^2 + s_4^2 \cdot s_2}}\right)^2}} \cdot \frac{s_2^2 + s_3^2 - s_1^2 - s_4^2}{2\sqrt{s_1^2 + s_4^2 \cdot s_2^2}} \cdot v_s \tag{4}$$

Once propellers start rotating to generate lift, the reaction force is transmitted through the telescopic mechanism to the central motor, as illustrated in Figure 3b. It should be noted that the position of intersection point *P* changes with varying lengths of arm *AM* and support rod *BN*, reflecting different correlations between propeller thrust and central motor load. Therefore, to prevent overheating or even damage to the central motor due to excessive loading; the relationship between the load and thrust represented by structural dimensions is firstly derived, upon which the optimization of the force ratio would then be conducted.

Drones 2025, 9, 736 9 of 22

Thrust F_0 remains perpendicular to arm AM under any reconfiguration angle ζ , resulting in a tensile force F_{BN} acting on pinned support B. Given the small dimension of the connector, neglect length s_4 and angle β in the following analysis for simplicity. Thus, the tensile force at support B is approximated to be exerted along line BD, which is denoted as F_{BD} . Neglect gravity and friction and set up a Cartesian coordinate system; the angle between force F_A and horizontal direction is expressed as

$$\gamma = \tan^{-1} \frac{\sin \zeta (\tan \zeta + \tan \alpha)(L - s_1) - L\sin \zeta \tan \alpha + L\cos \zeta}{-s_1 \sin \zeta + (L - s_1)\cos \zeta \tan \alpha + L\sin \zeta \tan \zeta \tan \alpha}$$
 (5)

together with forces at hinges

$$F_A = -\frac{\cos(\alpha + \zeta)}{\cos(\alpha + \gamma)} F_0 \tag{6}$$

$$F_{BD} = \frac{\sin(\zeta - \gamma)}{\cos(\alpha + \gamma)} F_0 \tag{7}$$

At hinge B, the tensile force F_{BD} , the constraint force from the pinned support, which can be decomposed into a horizontal component F_H and a vertical component F_I , are in equilibrium. Moreover, since load F of the central motor under a one-sided lift is the reaction force of force F_I , the force ratio of load F to lift force F_0 can be represented as

$$\frac{F}{F_0} = \frac{\sin(\zeta - \gamma)\cos\alpha}{\cos(\alpha + \gamma)} \tag{8}$$

Due to the symmetry of the quadcopter, the horizontal constraint force F_H at opposite hinges is of the same magnitude and opposite directions, thus resulting in zero net force on the central motor, which is neglected. For detailed derivation of Equations (5)–(8), please refer to Appendix A.1.

In Equation (8), both angles α and γ are functions of arm and support rod lengths. Therefore, by substituting Equations (2) and (5), and taking nondimensionalized ratios s_1/L and s_3/L as optimization variables, the force ratio of F to F_0 under a different reconfiguration angle ζ is optimized. The optimization aimed to minimize the maximum value of this force ratio across the full morphing range. A key kinematic constraint, $s_3 > s_1$ (simplified from $s_3 > \sqrt{s_1^2 + s_4^2}$), was applied to prevent the mechanism from reaching a dead point. Considering the overall size of our quadcopter, the arm length L is set to be 25 cm. The optimization results are shown in Table 4, and the variation in force ratio to the reconfiguration angle is illustrated in Figure 4. It can be seen that the optimization not only significantly reduces the force acting on the central motor at each reconfiguration angle, with a maximum force ratio drop of 65%, but also smooths the force within the full reconfiguration range, thereby improving the operational environment of the central motor during flight. Moreover, after optimization, the maximum shrinkage rate of the drone, which reflects the area change when ζ varies from 30° to 90°, is measured to be about 55%, showing the large-scale reconfigurability of our drone.

Table 4. Comparison of structural dimensions.

Parameter	Dimension Before Optimization (cm)	Dimension After Optimization (cm)
Hinge distance s_1	5	12
Support rod length s_3	12.5	18
Arm length L	25	25

Drones 2025, 9, 736 10 of 22

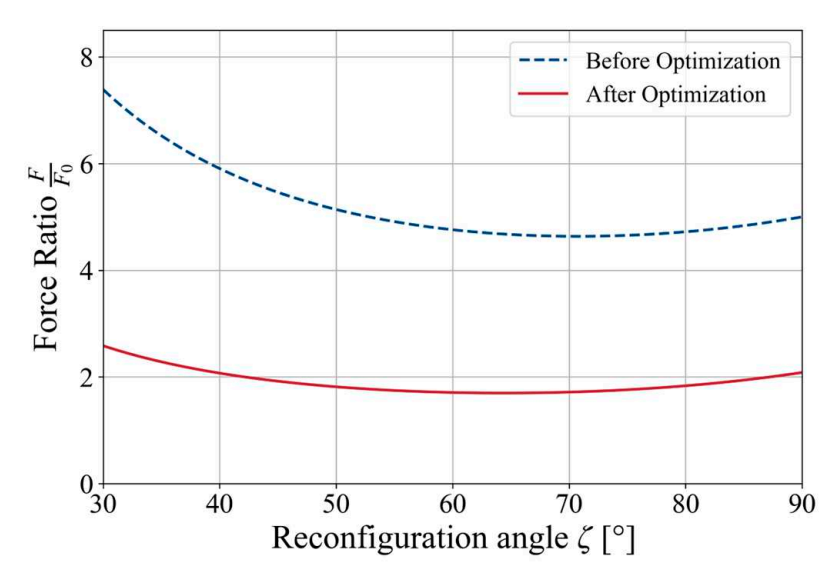


Figure 4. Force ratio comparison.

2.2.2. Inertial Parameters Change During Reconfiguration Process

During the reconfiguration process, the inertial parameters change with angle ζ , significantly affecting the control law of the quadcopter. By extracting the parameters at characteristic angles in SolidWorks 2022 SP 5.0 and fitting them with polynomial functions, the variation in the parameters with the reconfiguration angle ζ is depicted in Figure 5.

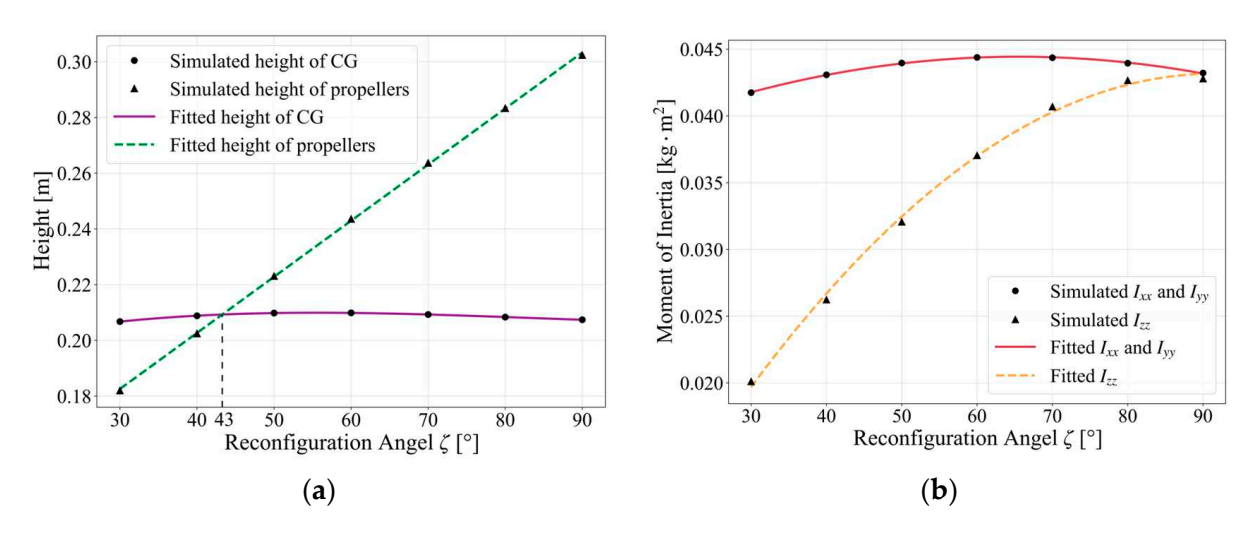


Figure 5. Inertial parameters varying with the reconfiguration angle: (a) heights of central gravity (CG) and propellers; (b) principal moments of inertia.

Figure 5a illustrates the change in central gravity (CG) and propeller height with respect to reconfiguration angle ζ , where the reference is taken from the bottom plane of the telescopic mechanism. The results reveal that the reconfiguration has little impact on the height of CG, which stays around 0.21 m, whereas the height of the propellers decreases dramatically as ζ decreases due to the inward rotation of arms to the main body. According to symmetry, the height of the center of lift (CL) is consistent with the propeller height. Therefore, CL is higher than CG under large reconfiguration angles, indicating the statically stable property of the quadcopter. As ζ decreases, the height of CL gradually comes closer to that of CG, and the quadcopter exhibits greater maneuverability. The heights take equal value at $\zeta = 43^\circ$, and the quadcopter is statically unstable when ζ is smaller than 43°. This introduces a fundamental trade-off between inherent stability and agility, a phenomenon well-documented in UAVs undergoing morphological or mass-distribution

Drones 2025, 9, 736 11 of 22

changes [22,23]. The instability at low ζ values increases control difficulty but is the key to enabling high-agility maneuvers, such as rapid traversal through narrow gaps.

Figure 5b displays the drone's moment of inertia about the axis defined in Figure 6 with angle ζ . $I_{xx} = I_{yy}$ holds for any value of ζ due to the drone's symmetry. As seen in the figure, the moments of inertia around the x and y axes first increase and subsequently decrease as ζ decreases, while the value of the moment of inertia around the z axis reduced significantly due to the arms' retraction. The results also indicate the strong directional maneuverability under small reconfiguration angles.

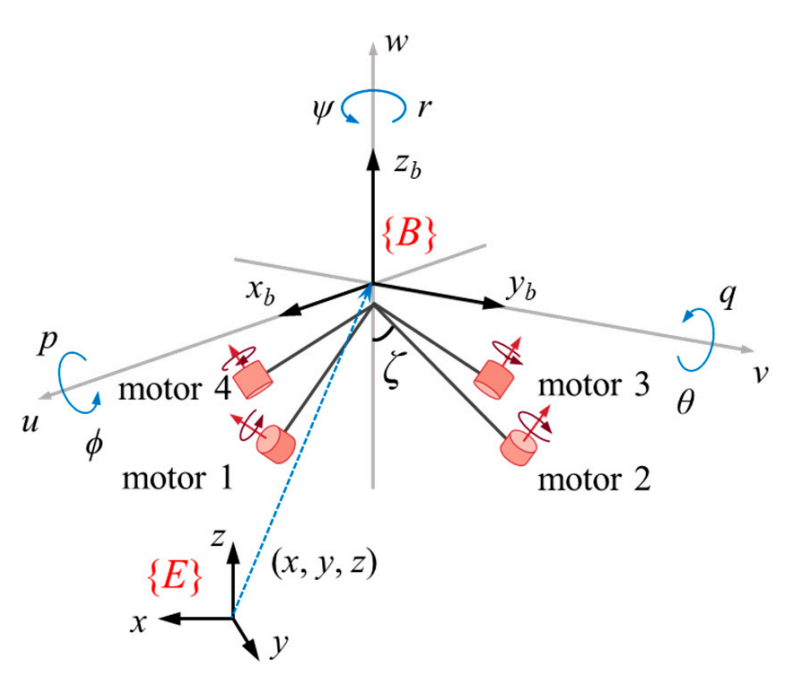


Figure 6. Coordinate system definition of reconfigurable drone.

The fitted equations of the quadrotor's inertial parameters with respect to ζ are shown below as

$$\begin{cases} H_{CG} = 4.58 \times 10^{-8} \cdot \zeta^{3} - 1.13 \times 10^{-5} \cdot \zeta^{2} + 8.35 \times 10^{-4} \cdot \zeta + 0.191 \text{ [m]} \\ H_{CL} = 2.01 \times 10^{-3} \cdot \zeta + 0.122 \text{ [m]} \\ I_{xx} = I_{yy} = -2.11 \times 10^{-6} \cdot \zeta^{2} + 2.76 \times 10^{-4} \cdot \zeta + 0.0354 \text{ [kg·m}^{2}] \\ I_{zz} = -6.19 \times 10^{-6} \cdot \zeta^{2} + 1.13 \times 10^{-3} \cdot \zeta - 8.75 \times 10^{-3} \text{ [kg·m}^{2}] \end{cases}$$
(9)

3. Control Design

3.1. Dynamic Model

Compared with traditional multicopters, our reconfigurable drone induces the angle ζ between the arms and the central axis of the main body as an additional control variable. This results in a unique set of state equations of body velocity $\mathbf{v} = \begin{bmatrix} u & v & w \end{bmatrix}^T$, world position $\mathbf{p} = \begin{bmatrix} x & y & z \end{bmatrix}^T$, body angular velocity $\mathbf{w} = \begin{bmatrix} p & q & r \end{bmatrix}^T$, and Euler angle $\mathbf{\Phi} = \begin{bmatrix} \phi & \theta & \psi \end{bmatrix}^T$, as shown in Equations (10)–(13), respectively. \mathbf{F} is the thrust force vector, and \mathbf{M} represents the thrust moment, whose derivations and expressions are demonstrated in detail in Appendix A.2, together with the rotational matrix \mathbf{R}^{BE} from the inertial frame to

Drones 2025, 9, 736 12 of 22

the body frame and transformation matrix H [8,24]. The gravity in body frame $g^B = R^{BE}g$, where g is the gravity in the inertial frame, which takes $g = \begin{bmatrix} 0 & 0 & -9.8 \text{ m/s}^2 \end{bmatrix}^T$.

$$\dot{v} = \frac{1}{m}F + g^{B} - \omega \times v = \begin{bmatrix} \dot{u} & \dot{v} & \dot{w} \end{bmatrix}^{T}$$
(10)

$$\dot{p} = R^{\text{BE}}v = \begin{bmatrix} \dot{x} & \dot{y} & \dot{z} \end{bmatrix}^{\text{T}} \tag{11}$$

$$\dot{\omega} = I^{-1}(M - \omega \times I\omega) = \begin{bmatrix} \dot{p} & \dot{q} & \dot{r} \end{bmatrix}^{\mathrm{T}}$$
(12)

$$\dot{\boldsymbol{\Phi}} = \boldsymbol{H}\boldsymbol{\omega} = \begin{bmatrix} \dot{\boldsymbol{\phi}} & \dot{\boldsymbol{\theta}} & \dot{\boldsymbol{\psi}} \end{bmatrix}^{\mathrm{T}} \tag{13}$$

In addition, I represents the mass moment of the inertia matrix, which is a single-valued function of angle ζ . Since the moments of inertia about the principal axes are substantially greater than the products of inertia, the matrix can be simplified as a diagonal matrix [25] as

$$I = I(\zeta) = \operatorname{diag}(I_{xx}, I_{yy}, I_{zz}) \tag{14}$$

where the expressions of I_{xx} , I_{yy} , and I_{zz} are shown in Equation (9).

3.2. PID Attitude-Position Control

A set of PID controllers is designed for the attitude-position control, which takes the changing parameters into account when morphing. The framework was chosen for its computational efficiency and straightforward implementation using prevalent flight controllers like Pixhawk. While advanced control strategies (e.g., adaptive or sliding mode control) could be adopted for better controllability, the PID controller is demonstrated to be sufficient for achieving stable and accurate flight control, as evidenced by the simulation results in Section 3.3. Although the controller itself is not the core contribution of this work, it serves as a practical and sufficient solution to demonstrate the controllability of the proposed platform. The control algorithm predominantly retains the classical architecture, while incorporating modifications based on the unique dynamic characteristics of the reconfigurable drone [26].

Distinct from conventional quadcopters, the trajectory planning of the proposed drone can fully leverage its morphing ability. Especially in those cases when conventional drones have to detour due to narrow gaps during flight, it enables direct traverse through structural reconfiguration. However, such capabilities can induce thrust force components along both x and y axes in the body frame. Consequently, under the given desired yaw attitude $\psi_{\rm c}(t)$, the dynamic equations for solving the commanded pitch attitude $\theta_{\rm c}$ and roll attitude $\phi_{\rm c}$ should be written as

$$\begin{cases} a_{c1}\cos\theta_{c}\cos\psi_{c} + a_{c2}\cos\theta_{c}\sin\psi_{c} - (a_{c3} + g)\sin\theta_{c} - \frac{F_{x}}{m} = 0\\ a_{c1}\sin\psi_{c} - a_{c2}\cos\psi_{c} - \frac{F_{z}}{m}\sin\phi_{c} + \frac{F_{y}}{m}\cos\phi_{c} = 0\\ a_{c1}^{2} + a_{c2}^{2} + (a_{c3} + g)^{2} = \left(\frac{F_{x}}{m}\right)^{2} + \left(\frac{F_{y}}{m}\right)^{2} + \left(\frac{F_{z}}{m}\right)^{2} \end{cases}$$
(15)

where a_{c1} , a_{c2} , and a_{c3} are the virtual control vector components in x, y and z axis, respectively, which is calculated in the PID position controller, and F_x , F_y , and F_z are the commanded thrust vector components in x, y, and z directions, respectively. Given this underdetermined system where three equations are to solve five commanded unknowns

Drones 2025, 9, 736 13 of 22

 $(F_x, F_y, F_z, \theta_c, \text{ and } \phi_c)$, we assume $F_x = F_y = 0$ holds in all cases, thus simplifying the equations and deriving the expressions of θ_c , ϕ_c , and F_z as

$$\begin{cases} \theta_{c} = \tan^{-1}\left(\frac{a_{c1}\cos\psi_{c} + a_{c2}\sin\psi_{c}}{a_{c3} + g}\right) \\ \phi_{c} = \sin^{-1}\left(\frac{a_{c1}\sin\psi_{c} - a_{c2}\cos\psi_{c}}{\sqrt{a_{c1}^{2} + a_{c2}^{2} + (a_{c3} + g)^{2}}}\right) \\ F_{z} = m[a_{c1}(\sin\theta_{c}\cos\psi_{c}\cos\phi_{c} + \sin\psi_{c}\sin\phi_{c}) \\ + a_{c2}(\sin\theta_{c}\sin\psi_{c}\cos\phi_{c} - \cos\psi_{c}\sin\phi_{c}) + (a_{c3} + g)\cos\theta_{c}\cos\phi_{c}] \end{cases}$$
(16)

After obtaining the z component of the thrust vector, the commanded thrust of each propeller is computed based on the allocation matrix under the current configuration. The results are utilized to further obtain the actual x and y components of the thrust vector, which contribute to the real dynamics of the drone. Although the above simplifications ignore the control benefit gained from force components F_x and F_y , and might amplify the control error, it significantly simplifies the results and avoids the multiple-solutions problem when solving Equation (15) directly. Moreover, simulations in Section 3.3 will demonstrate favourable control results of controllers designed based on this idea even when reconfigurations are employed.

In addition, it is crucial to note that the actual force vector *F* and moment vector *M* should consider the actuator limits. Consequently, the propeller thrusts computed from the ideal control force and moment (via an allocation matrix) must be constrained within the feasible domain, which subsequently allows the derivation of the actual achievable output force and moment through inverse calculation.

3.3. Simulation Results and Discussions

3.3.1. Trajectory Tracking

By implementing a simulation program in MATLAB R2024a, the control algorithm's performance under various operating conditions is evaluated. Discrete target points are defined based on the prescribed tracking trajectory, and a time step of 0.01 s is selected for tracking calculations. After deriving the state variable derivatives from Equations (10)–(13), the ode45 solver was employed to numerically integrate the system dynamics. In addition, dual constraints on the position and velocity with tolerances of 0.01 m and 0.01 m/s, respectively, are applied for a termination check, guaranteeing the accurate completion of the tracking task.

An "8"-shaped curve is selected for the simulation of path tracking, which is denoted by $x_r = r\cos(\omega_r t)/(1+\sin^2(\omega_r t))$, $y_r = r\sin(\omega_r t)\cos(\omega_r t)/(1+\sin^2(\omega_r t))$, and $z_r = t/5$ (when $t \le T/2$), (T-t)/5 (when $T/2 < t \le T$), with r = 5 m, $\omega_r = 2\pi/25$ rad/s, and total time T = 25 s. The quadcopter is initialized in a folded configuration, with the reconfiguration angle $\zeta = 30^\circ$, and takes off from the ground. Once taking off, the drone starts to track the predefined path, with central sleeves simultaneously shortening uniformly to deploy the arms. When angle ζ reaches 90°, the drone will maintain the deployed configuration and track the remaining path until completed. Several performance indicators are chosen as the criteria to evaluate the path tracking performance [27]. The mean square error (*MSE*),

$$MSE = \frac{1}{N} \sum_{i=1}^{N} e_i^2$$
, for $i = \{1, 2, ..., N\}$ (17)

Drones 2025, 9, 736 14 of 22

the root mean square error (RMSE),

$$RMSE = \sqrt{\frac{1}{N} \sum_{i=1}^{N} e_i^2}, \text{ for } i = \{1, 2, \dots, N\}$$
 (18)

the integral absolute error (IAE),

$$IAE = \int_0^T |e(t)| dt \tag{19}$$

the integral squared error (ISE),

$$ISE = \int_0^T e^2(t) dt \tag{20}$$

and the integral time absolute error (ITAE),

$$ITAE = \int_0^T |e(t)| t dt \tag{21}$$

where N is the number of data points, $e_i = \|p_i - p_{i,\text{des}}\|$, $e(t) = \|p(t) - p_{\text{des}}(t)\|$, where $p_i(p(t))$ is the actual position of the drone, and $p_{i,\text{des}}(p_{\text{des}}(t))$ is the desired trajectory.

Firstly, based on Equation (4), the rotational speed ω_{arm} of the arms during the deployment process is calculated, as shown in Figure 7. The total reconfiguration time for deployment from $\zeta=30^\circ$ to 90° takes about 3 s. During the process, the arms' rotational speed varies nonlinearly over time. Initially, under small angles, the rotational speed is relatively high but decreases rapidly as the reconfiguration angle increases. Finally, the rate of change comes close to zero, and at time t=2.65 s, where $\zeta\approx85^\circ$ (marked by a red "x" in the figure), the speed reaches its minimum value.

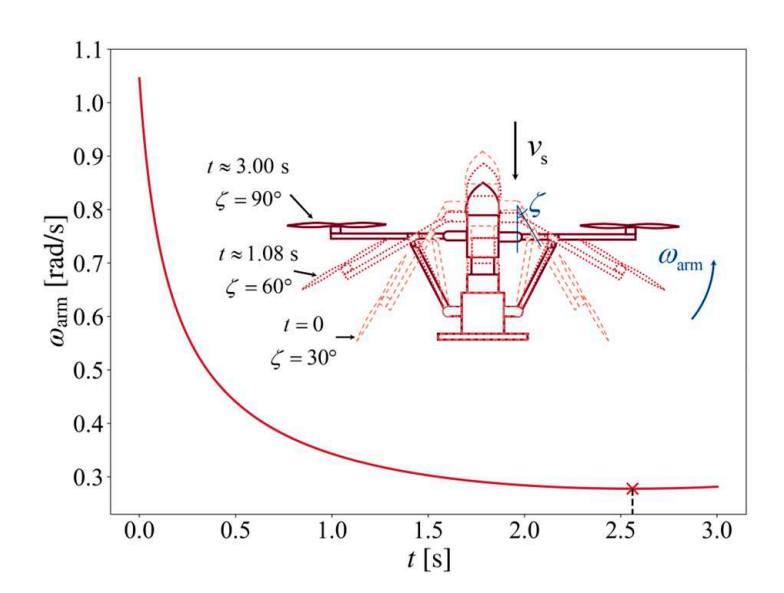


Figure 7. Angular velocity with constant sleeve contraction speed.

Subsequently, the drone's inertial parameters are further derived based on the angular speed change, and the drone's flight tracking the "8"-shaped trajectory is conducted numerically, which are shown in Figure 8a. To rigorously evaluate the robustness of the controllers, wind disturbances are further introduced, comprising a constant wind velocity of $v_{cw} = [v_{cwx}, v_{cwy}, v_{cwz}]^T = [5 \text{ m/s}, 5 \text{ m/s}, 0]^T$ combined with sinusoidal gusts defined as $v_g = [v_{gx}, v_{gy}, v_{gz}]^T = [V_g \sin(\omega_g t + 0.1), V_g \sin(\omega_g t + 0.3), 0.5V_g \sin(\omega_g t + 0.5)]^T$,

Drones 2025, 9, 736 15 of 22

where $V_{\rm g}$ = 10 m/s and $\omega_{\rm g}$ = 0.8 π rad/s. The trajectory tracking results under these wind conditions are depicted in Figure 8b. As evidenced by the performance metrics in Table 5, the drone maintains robust wind resistance and precise trajectory tracking, validating the controller's satisfactory effectiveness. This result further confirms that the modelling simplification from Equations (15) and (16) yields acceptable errors even under significant external disturbances.

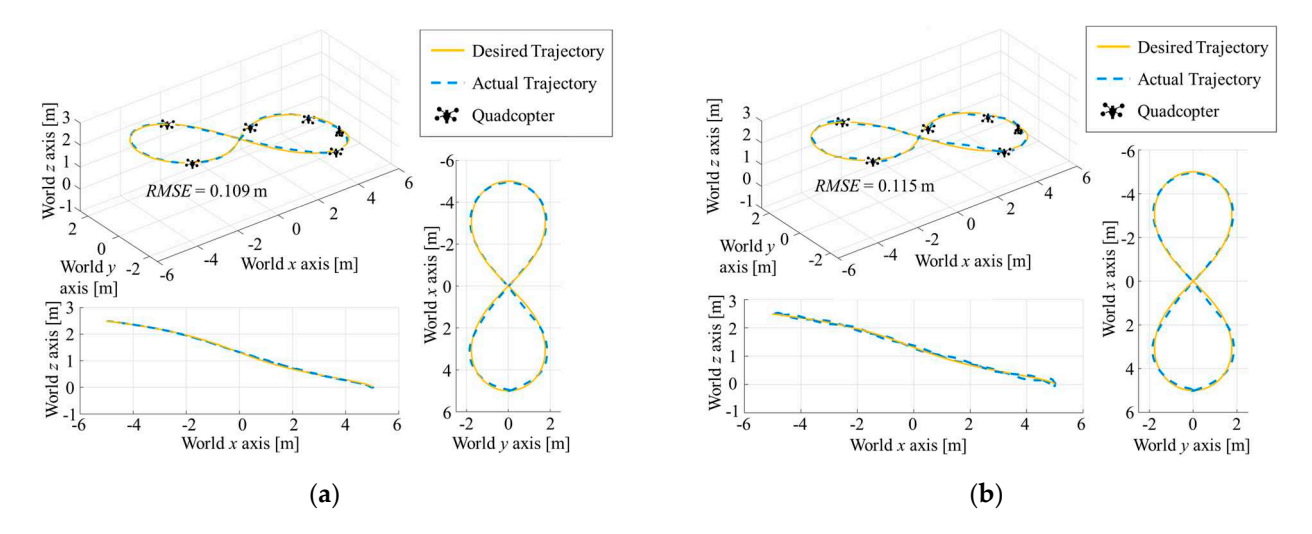


Figure 8. The "8"-shaped trajectory tracking simulation: (a) without wind disturbances; (b) with wind disturbances.

Condition	Performance Indicators				
Without wind disturbances	MSE/m ²	<i>RMSE/</i> m	<i>IAE</i> /m⋅s	<i>ISE</i> /m ² ⋅s	<i>ITAE</i> /m⋅s ²
	1.18×10^{-2}	0.109	2.57	0.310	34.8
With wind disturbances	MSE/m ²	<i>RMSE/</i> m	<i>IAE</i> /m⋅s	<i>ISE</i> /m²⋅s	<i>ITAE</i> /m⋅s ²
	1.33×10^{-2}	0.115	3.18	0.366	50.6

Table 5. Quantitative results of the "8"-shaped trajectory tracking.

3.3.2. Traversing a Long Narrow Gap

Simulations are further performed for a case to traverse a long narrow gap, as shown in Figure 9a. In this case, three obstacles are positioned along the drone's flight path connecting the starting point and the destination, forming a long narrow gap between them. Assume the drone takes off from the ground in a fully deployed configuration, i.e., $\zeta=90^\circ$, and flies toward the entry of the gap. To minimize the traversing time, arms' retraction is initiated 3 s before the traversal, ensuring the drone completes reconfiguration precisely at the gap entrance and maintaining $\zeta=30^\circ$ during traversal. Once flying out of the gap, the arms start to re-deploy to $\zeta=90^\circ$, while the drone simultaneously flies to the destination and lands on the ground. The simulation results are shown in Figure 9b. The distance of the total flight path is 40.6 m, with a flying duration of 17.6 s, and the performance indicators are presented in Table 6.

Drones 2025, 9, 736 16 of 22

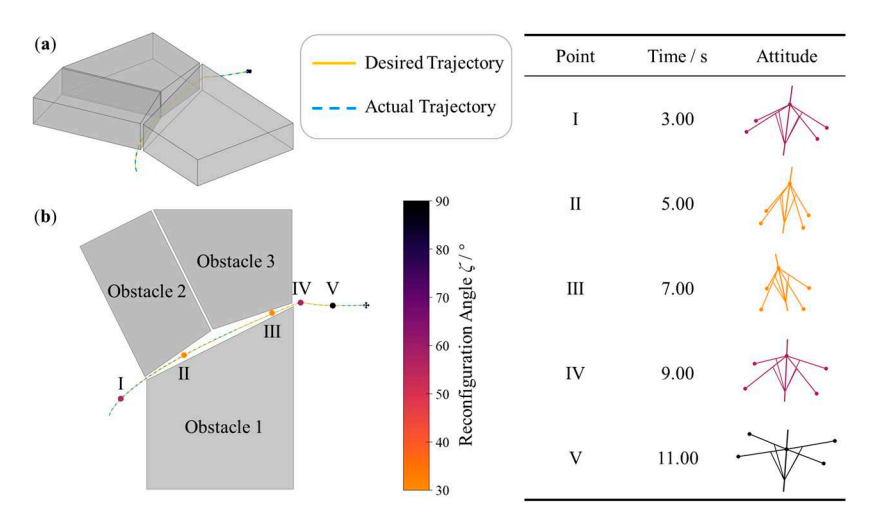


Figure 9. Long narrow gap passing simulation: (a) scene; (b) results and insights of feature points.

Table 6. Quantitative results of traversing a long narrow gap.

MSE/m ²	RMSE/m	<i>IAE</i> /m⋅s	<i>ISE</i> /m ² ⋅s	ITAE/m·s ²
7.26×10^{-3}	0.0852	1.45	0.181	10.9

To further demonstrate our reconfigurable drone's capability of reducing the arrival time by taking full advantage of its reconfigurability, the following scenario is considered: a search-and-rescue unit requires an urgent aerial survey of a disaster area, where multiple tall obstacles are along the way. Assume there are two options (as shown in Figure 10a):

- Plan A: Shorter path requiring traversing long narrow gaps;
- Plan B: Detouring around the obstacles with a longer route.

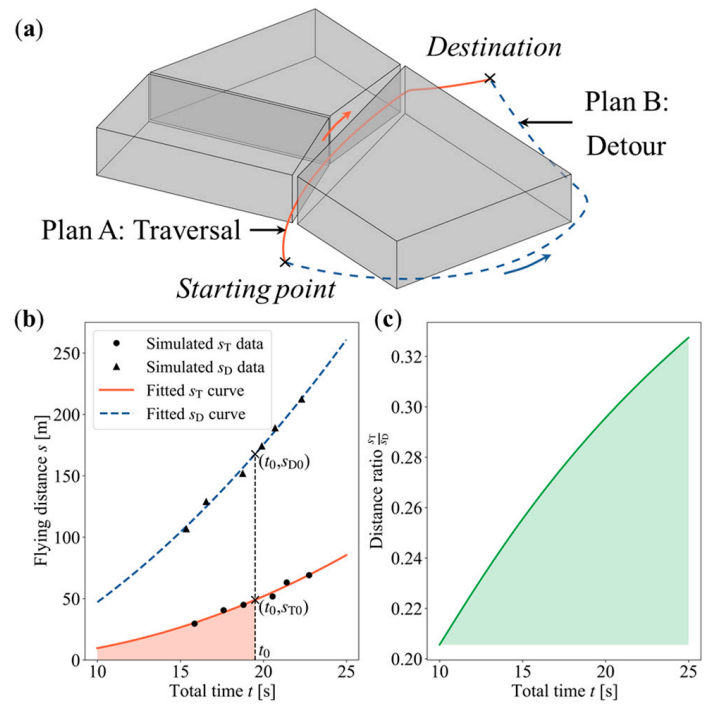


Figure 10. Comparison of two strategies: (a) case visualization; (b) *s-t* curve comparison; (c) distance ratio curve.

Drones 2025, 9, 736 17 of 22

Except for periods of taking off and landing, the flying altitude of two trajectories remains the same. Moreover, Plan A adopts the aforementioned strategy, which ensures the drone to be fully folded precisely at the gap entrance, maintaining $\zeta=30^\circ$ for traversal, while re-deploying to $\zeta=90^\circ$ and maintaining the configuration until reaching the destination. In Plan B, the drone remains fully deployed ($\zeta=90^\circ$) throughout the flight. To evaluate the time-optimal solution between two routes, simulations are conducted by varying the dimensions of the obstacles. This allowed us to modify the distances for both traversal and detour while maintaining a consistent path-tracking *RMSE* of 0.08 m, along with unchanged take-off and landing distances. The results are shown in Figure 10b, and the traversal-to-detour distance ratio versus the total flight time is presented in Figure 10c.

As shown in Figure 10b, if the detour distance s_{D0} and the corresponding duration t_0 are known, a vertical line passing through this point can be further drawn, which intersects the fitted traversal curve at (t_0, s_{T0}) . The results then yield the following conclusions:

- If the actual traversal distance $s_T < s_{T0}$, which is the case inside the colour-filled region in Figure 10b, selecting Plan A for traversal will reduce the arrival time;
- If $s_{T0} < s_T \le s_{D0}$, selecting Plan B with detouring will save time.

Additionally, it can be seen from Figure 10c that as both traversal and detour distances increase, the distance ratio between the two strategies also increases at the same total duration. The colour-filled area under the curve indicates cases when a traversal flight saves mission time. The results indicate that, when the flying distance becomes longer, the traversal flight will demonstrate a time-saving advantage over a larger range.

It is important to note that the time-optimal analysis presented here serves as a preliminary comparison. The folded configuration likely incurs penalties in aerodynamic efficiency and flight stability, which may necessitate slower flight speeds. Furthermore, the energy cost of the reconfiguration actuator itself is not considered. Therefore, the identified time-saving regime illustrates scenarios where the advantage of a significantly shorter path may overcome these drawbacks.

4. Conclusions

In this study, biomimetically inspired by the morphology and swimming pattern of jellyfish, a novel reconfigurable quadcopter driven by a central motor was investigated. This design provided a possible solution to achieve significant reconfiguration with a minimal number of actuators. By integrating a crank-slider mechanism to convert lead screw translation to arms' rotation, continuous retraction and deployment of arms were realized, enabling the drone to maintain any configuration as required. The design incorporated three-stage nested sleeves, ensuring structural simplicity and compactness. To enhance overall reliability and reduce power consumption, the key dimensions of the drone were optimized, reducing the maximum load on the central servomotor by approximately 65%. The arms' rotational speed and inertial parameters were then derived based on the optimized parameters. A set of PID controllers was further designed considering the unique dynamics and parameters for the drone's flight control, whose performance was validated through MATLAB numerical simulations. The simulation results demonstrate the drone's capability for precise trajectory tracking during the morphing process and in a folded configuration. Moreover, the drone could traverse narrow gaps through reconfiguration under specific conditions, reducing the time to reach destinations.

Despite the promising simulation results, this study has several limitations that present opportunities for future research. Firstly, the use of a PID controller, while effective in simulation for demonstrating the platform's basic controllability, provides limited methodological novelty. Its efficacy in real-world scenarios with external disturbances requires further

Drones 2025, 9, 736 18 of 22

validation. The simplifying assumption of zero lateral thrust components ($F_x = F_y = 0$) also impedes the full use of aggressive maneuvering capabilities inherent to the tilting-arm design. Future work will therefore explore advanced model-based control strategies, such as adaptive or sliding mode control, to enhance robustness across all configurations and explicitly manage the stability transition that occurs near $\zeta = 43^{\circ}$.

Secondly, the presented gap-traversal simulations rely on predefined trajectories and perfect environmental knowledge. To achieve true autonomy, the integration of onboard sensors, such as a 3D LiDAR, with real-time motion planning algorithms is essential for enabling the drone to perceive and navigate unknown, constrained spaces dynamically.

Thirdly, the mechanical design, particularly the nested telescopic sleeves and lead screw mechanism, introduces potential failure points, including the risk of jamming and limited actuation speed. Preliminary ground tests (see Supplementary Video S4) have successfully demonstrated the basic functionality of the mechanism. Building upon this proof-of-concept, our immediate future work will prioritize the development of instrumented prototypes to quantitatively characterize actuation forces, reconfiguration speed, and structural dynamics. In parallel, further simulations will be conducted, including finite element analysis (FEA) of structural stresses during morphing and a detailed investigation into coupling between reconfiguration and flight stability. These steps, coupled with rigorous hardware-in-the-loop (HIL) tests, are crucial for validating the structural reliability and advancing towards real-world flight demonstrations.

Supplementary Materials: The following supporting information can be downloaded at https://www.mdpi.com/article/10.3390/drones9110736/s1, Video S1: Exploded View of the Prototype Design. Video S2: "8" shaped Trajectory Tracking Simulation. Video S3: Long Narrow Gap Passing Simulation. Video S4: Preliminary Ground Tests.

Author Contributions: Conceptualization, Z.W., K.H., and J.Z.; methodology, Z.W., K.H., and J.Z.; software, Z.W.; validation, Z.W. and K.H.; formal analysis, Z.W.; investigation, Z.W. and K.H.; resources, Z.W. and K.H.; data curation, Z.W.; writing—original draft preparation, Z.W.; writing—review and editing, Z.W., K.H., and J.Z.; visualization, Z.W.; supervision, J.Z.; project administration, J.Z.; funding acquisition, J.Z. All authors have read and agreed to the published version of the manuscript.

Funding: This project was funded by the National Natural Science Foundation of China (Grant No. 92271104, 12102017) and the Beijing Natural Science Foundation (Grant No. 1232014).

Data Availability Statement: The original contributions presented in this study are included in the paper/Supplementary Material. Further inquiries can be directed to the corresponding author.

Conflicts of Interest: The authors declare no conflicts of interest.

Appendix A Detailed Derivation of Formulas

Appendix A.1 Derivation of Force Ratio of Central Motor Axial Force to Lift Force

When conducting the dimensional optimization of our reconfigurable drone, the principle of three-force member equilibrium is employed to determine the force direction at hinge A. The analytical method is further applied to obtain forces acting on joints and components, respectively. As stated in the main context, length s_4 and angle β are neglected, thus the tensile force at hinge B is approximated to act along the direction of BD, which is denoted as F_{BD} . Neglect the gravity of bars and friction forces, a Cartesian coordinate system is established, as illustrated in Figure 3b.

Since points *A* and *M* lie on the positive *y*-axis and *x*-axis, respectively, their coordinates can be obtained as

Drones 2025, 9, 736 19 of 22

$$A(0, L\cos\zeta), M(L\sin\zeta, 0)$$

From the geometrical relationships, the coordinate of point *D* is

$$D(s_1\sin\zeta,(L-s_1)\cos\zeta)$$

Thus, functions of lines MP and DP are

$$MP : y = x \tan \zeta - L \sin \zeta \tan \zeta$$

$$DP: y = \frac{1}{\tan \alpha} (x - s_1 \sin \zeta) + (L - s_1) \cos \zeta$$

Solving these two equations simultaneous yields the coordinate of point *P* as

$$x_P = \frac{-s_1 \sin \zeta + (L - s_1) \cos \zeta \tan \alpha + L \sin \zeta \tan \zeta \tan \alpha}{\tan \alpha \tan \zeta - 1} \\ y_P = \frac{\sin \zeta (\tan \zeta + \tan \alpha)(L - s_1)}{\tan \alpha \tan \zeta - 1}$$

From the coordinates of points *A* and *P*, the slope of line *AP* is found as

$$k_{AP} = \frac{\sin\zeta(\tan\zeta + \tan\alpha)(L - s_1) - L\sin\zeta\tan\alpha + L\cos\zeta}{-s_1\sin\zeta + (L - s_1)\cos\zeta\tan\alpha + L\sin\zeta\tan\zeta\tan\alpha}$$

In addition,

$$k_{AP} = \tan \gamma$$

Therefore, the angle between force F_A and horizontal direction is obtained as

$$\gamma = \tan^{-1} \frac{\sin \zeta (\tan \zeta + \tan \alpha)(L - s_1) - L\sin \zeta \tan \alpha + L\cos \zeta}{-s_1 \sin \zeta + (L - s_1)\cos \zeta \tan \alpha + L\sin \zeta \tan \zeta \tan \alpha}$$
(A1)

From the static equilibrium of arm AM, it follows that

$$\begin{cases} F_A \cos \gamma - F_{BD} \sin \alpha + F_0 \cos \zeta = 0 \\ F_A \sin \gamma - F_{BD} \cos \alpha + F_0 \sin \zeta = 0 \end{cases}$$

with the solutions of the force F_A at hinge A and F_{BD} as

$$\begin{cases} F_A = -\frac{\cos(\alpha + \zeta)}{\cos(\alpha + \gamma)} F_0 \\ F_{BD} = \frac{\sin(\zeta - \gamma)}{\cos(\alpha + \gamma)} F_0 \end{cases}$$
(A2)

At pinned support B, the tension F_{BD} and the constraint force are in equilibrium, which can be decomposed as a horizontal constraint force F_H and a vertical force F', resulting in

$$\begin{cases} F_{BD}\sin\alpha - F_{H} = 0\\ F_{BD}\cos\alpha - F' = 0 \end{cases}$$

which can be solved as

$$\begin{cases} F_{\rm H} = \frac{\sin(\zeta - \gamma)\sin\alpha}{\cos(\alpha + \gamma)} F_0 \\ F' = \frac{\sin(\zeta - \gamma)\cos\alpha}{\cos(\alpha + \gamma)} F_0 \end{cases}$$
 (A3)

Since the axial load of the central motor *F* is the reaction force of the constraint force *F*′, according to Newton's third law, we have

$$F = F' = \frac{\sin(\zeta - \gamma)\cos\alpha}{\cos(\alpha + \gamma)}F_0 \tag{A4}$$

Drones 2025, 9, 736 20 of 22

or expressing in a nondimensionalized way of

$$\frac{F}{F_0} = \frac{\sin(\zeta - \gamma)\cos\alpha}{\cos(\alpha + \gamma)} \tag{A5}$$

Especially, consider the case when three forces are parallel with each other. At this moment, $\alpha + \zeta = \pi/2$, $\gamma = \zeta$ and $P = P_{\infty}$. Therefore, the equilibrium equations become

$$\begin{cases} F_0 + F_A - F_{BD} = 0 \\ F_0(L - s_1) - F_A s_1 = 0 \end{cases}$$

which can be solved as

$$\begin{cases} F_A = \frac{L - s_1}{s_1} F_0 \\ F_{BD} = \frac{L}{s_1} F_0 \end{cases}$$
 (A6)

Constraint forces and the axial load of the central motor are further solved to be

$$\begin{cases} F_{H} = \frac{L\sin\alpha}{s_{1}} F_{0} \\ F = F' = \frac{L\cos\alpha}{s_{1}} F_{0} \end{cases}$$
 (A7)

Appendix A.2 Control Dynamics Derivation

It is assumed that the thrust coefficient c_T and the torque coefficient c_Q are independent of the reconfiguration angle ζ [28], the thrust vector is derived as

$$F = \begin{bmatrix} c_{\rm T}(\omega_{\rm m1}^2 - \omega_{\rm m3}^2)\cos\zeta \\ c_{\rm T}(\omega_{\rm m2}^2 - \omega_{\rm m4}^2)\cos\zeta \\ c_{\rm T}(\omega_{\rm m1}^2 + \omega_{\rm m2}^2 + \omega_{\rm m3}^2 + \omega_{\rm m4}^2)\sin\zeta \end{bmatrix}$$
(A8)

where $\omega_{\mathrm{m}i}$ is the rotational speed of brushless motor i in RPM (1 RPM = $\pi/30~\mathrm{rad\cdot s^{-1}}$). The thrust moment of our reconfigurable drone can be obtained as

$$\mathbf{M} = \begin{bmatrix} 0 & Lc_{\mathrm{T}} & 0 & -Lc_{\mathrm{T}} \\ -Lc_{\mathrm{T}} & 0 & Lc_{\mathrm{T}} & 0 \\ -c_{\mathrm{Q}}\sin\zeta & c_{\mathrm{Q}}\sin\zeta & -c_{\mathrm{Q}}\sin\zeta & c_{\mathrm{Q}}\sin\zeta \end{bmatrix} \begin{bmatrix} \omega_{\mathrm{m}1}^2 \\ \omega_{\mathrm{m}2}^2 \\ \omega_{\mathrm{m}3}^2 \\ \omega_{\mathrm{m}3}^2 \end{bmatrix} = \begin{bmatrix} Lc_{\mathrm{T}}\omega_{\mathrm{m}2}^2 - Lc_{\mathrm{T}}\omega_{\mathrm{m}4}^2 \\ -Lc_{\mathrm{T}}\omega_{\mathrm{m}1}^2 + Lc_{\mathrm{T}}\omega_{\mathrm{m}3}^2 \\ c_{\mathrm{Q}}(-\omega_{\mathrm{m}1}^2 + \omega_{\mathrm{m}2}^2 - \omega_{\mathrm{m}3}^2 + \omega_{\mathrm{m}4}^2)\sin\zeta \end{bmatrix}$$
(A9)

In addition, the rotational matrix from inertial frame to body frame R^{BE} is expressed as

$$R^{\text{BE}} = \begin{bmatrix} \cos \psi \cos \theta & \cos \psi \sin \theta \sin \phi - \sin \psi \cos \phi & \cos \psi \sin \theta \cos \phi + \sin \psi \sin \phi \\ \sin \psi \cos \theta & \sin \psi \sin \theta \sin \phi + \cos \psi \cos \phi & \sin \psi \sin \theta \cos \phi - \cos \psi \sin \phi \\ -\sin \theta & \cos \theta \sin \phi & \cos \theta \cos \phi \end{bmatrix}$$
(A10)

The transformation matrix H is expressed as

$$H = \begin{bmatrix} 1 & \tan\theta\sin\phi & \tan\theta\cos\phi \\ 0 & \cos\phi & -\sin\phi \\ 0 & \frac{\sin\phi}{\cos\theta} & \frac{\cos\phi}{\cos\theta} \end{bmatrix}$$
(A11)

Drones 2025, 9, 736 21 of 22

References

- 1. Quan, Q. Introduction to Multicopter Design and Control; Springer: Singapore, 2017.
- 2. Shafiee, M.; Zhou, Z.; Mei, L.; Dinmohammadi, F.; Karama, J.; Flynn, D. Unmanned Aerial Drones for Inspection of Offshore Wind Turbines: A Mission-Critical Failure Analysis. *Robotics* **2021**, *10*, 26. [CrossRef]
- 3. Videras Rodríguez, M.; Melgar, S.G.; Cordero, A.S.; Márquez, J.M.A. A Critical Review of Unmanned Aerial Vehicles (UAVs) Use in Architecture and Urbanism: Scientometric and Bibliometric Analysis. *Appl. Sci.* **2021**, *11*, 9966. [CrossRef]
- 4. Chyrva, I.; Jermy, M.; Strand, T.; Richardson, B. Evaluation of the Pattern of Spray Released from a Moving Multicopter. *Pest Manag. Sci.* **2023**, *79*, 1483–1499. [CrossRef] [PubMed]
- 5. Xing, S.; Zhang, X.; Tian, J.; Xie, C.; Chen, Z.; Sun, J. Morphing Quadrotors: Enhancing Versatility and Adaptability in Drone Applications—A Review. *Drones* **2024**, *8*, 762. [CrossRef]
- 6. Li, M. Beyond Conventional Drones: A Review of Unconventional Rotary-Wing UAV Design. *Drones* 2025, 9, 323. [CrossRef]
- Mowla, M.N.; Asadi, D.; Durhasan, T.; Jafari, J.R.; Amoozgar, M. Recent Advancements in Morphing Applications: Architecture, Artificial Intelligence Integration, Challenges, and Future Trends-A Comprehensive Survey. *Aerosp. Sci. Technol.* 2025, 161, 110102.
 [CrossRef]
- 8. Patnaik, K.; Zhang, W. Towards Reconfigurable and Flexible Multirotors: A Literature Survey and Discussion on Potential Challenges. *Int. J. Intell. Robot.* **2021**, *5*, 365–380. [CrossRef]
- 9. Ryll, M.; Bülthoff, H.H.; Giordano, P.R. First Flight Tests for a Quadrotor UAV with Tilting Propellers. In Proceedings of the 2013 IEEE International Conference on Robotics and Automation, Karlsruhe, Germany, 6–10 May 2013; pp. 295–302.
- 10. Kamel, M.; Verling, S.; Elkhatib, O.; Sprecher, C.; Wulkop, P.; Taylor, Z.; Siegwart, R.; Gilitschenski, I. The Voliro Omniorientational Hexacopter: An Agile and Maneuverable Tiltable-rotor Aerial Vehicle. *IEEE Robot. Autom. Mag.* **2018**, 25, 34–44. [CrossRef]
- 11. Zheng, P.; Tan, X.; Kocer, B.B.; Yang, E.; Kovac, M. TiltDrone: A Fully-actuated Tilting Quadrotor Platform. *IEEE Robot. Autom. Lett.* **2020**, *5*, 6845–6852. [CrossRef]
- 12. Lv, Z.Y.; Wu, Y.; Zhao, Q.; Sun, X.M. Design and Control of a Novel Coaxial Tilt-rotor UAV. *IEEE Trans. Ind. Electron.* **2021**, *69*, 3810–3821. [CrossRef]
- 13. Lv, Z.; Zhao, Q.; Sun, X.M.; Wu, Y. Finite-time Control Design for a Coaxial Tilt-rotor UAV. *IEEE Trans. Ind. Electron.* **2024**, 71, 16132–16142. [CrossRef]
- 14. Meiri, N.; Zarrouk, D. Flying STAR, a Hybrid Crawling and Flying Sprawl Tuned Robot. In Proceedings of the 2019 International Conference on Robotics and Automation (ICRA), Montreal, QC, Canada, 20–24 May 2019; pp. 5302–5308.
- 15. Mishra, S.; Patnaik, K.; Garrard, Y.Z.; Chase, Z.; Ploughe, M.; Zhang, W. Ground Trajectory Control of an Unmanned Aerial-ground Vehicle Using Thrust Vectoring for Precise Grasping. In Proceedings of the 2020 IEEE/ASME (AIM) International Conference on Advanced Intelligent Mechatronics, Boston, MA, USA, 6–9 July 2020; pp. 1270–1275.
- 16. Yang, J.; Zhu, Y.; Zhang, L.; Dong, Y.; Ding, Y. Sytab: A Class of Smooth-transition Hybrid Terrestrial/Aerial Bicopters. *IEEE Robot. Autom. Lett.* **2022**, *7*, 9199–9206. [CrossRef]
- 17. Tan, Y.H.; Chen, B.M. Design of a Morphable Multirotor Aerial-aquatic Vehicle. In Proceedings of the OCEANS 2019 MTS/IEEE SEATTLE, Seattle, WA, USA, 27–31 October 2019; pp. 1–8.
- 18. Yang, D.; Mishra, S.; Aukes, D.M.; Zhang, W. Design, Planning, and Control of an Origami-inspired Foldable Quadrotor. In Proceedings of the 2019 American Control Conference (ACC), Philadelphia, PA, USA, 10–12 July 2019; pp. 2551–2556.
- 19. Falanga, D.; Kleber, K.; Mintchev, S.; Floreano, D.; Scaramuzza, D. The Foldable Drone: A Morphing Quadrotor That Can Squeeze and Fly. *IEEE Robot. Autom. Lett.* **2019**, *4*, 209–216. [CrossRef]
- 20. Mintchev, S.; De Rivaz, S.; Floreano, D. Insect-inspired Mechanical Resilience for Multicopters. *IEEE Robot. Autom. Lett.* **2017**, 2, 1248–1255. [CrossRef]
- 21. Pastor, D.; Izraelevitz, J.; Nadan, P.; Bouman, A.; Burdick, J.; Kennedy, B. Design of a Ballistically-launched Foldable Multirotor. In Proceedings of the 2019 IEEE/RSJ International Conference on Intelligent Robots and Systems (IROS), Macau, China, 3–8 November 2019; pp. 5212–5218.
- Lee, S.; Giri, D.K.; Son, H. Modeling and Control of Quadrotor UAV Subject to Variations in Center of Gravity and Mass. In Proceedings of the 2017 14th International Conference on Ubiquitous Robots and Ambient Intelligence (URAI), Jeju, Republic of Korea, 28 June–1 July 2017; pp. 85–90.
- 23. Bucki, N.; Mueller, M.W. Design and Control of a Passively Morphing Quadcopter. In Proceedings of the 2019 International Conference on Robotics and Automation (ICRA), Montreal, QC, Canada, 20–24 May 2019; pp. 9116–9122.
- 24. Rubí, B.; Ruiz, A.; Pérez, R.; Morcego, B. Path-flyer: A Benchmark of Quadrotor Path Following Algorithms. In Proceedings of the 2019 IEEE 15th International Conference on Control and Automation (ICCA), Edinburgh, UK, 16–19 July 2019; pp. 633–638.
- 25. Desbiez, A.; Expert, F.; Boyron, M.; Diperi, J.; Viollet, S.; Ruffier, F. X-Morf: A Crash-separable Quadrotor That Morfs Its X-geometry In Flight. In Proceedings of the 2017 Workshop on Research, Education and Development of Unmanned Aerial Systems (RED-UAS), Linköping, Sweden, 3–5 October 2017; pp. 222–227.

Drones 2025, 9, 736 22 of 22

26. Zuo, Z. Trajectory Tracking Control Design with Command-filtered Compensation for a Quadrotor. *IET Contr. Theory Appl.* **2010**, 4, 2343–2355. [CrossRef]

- 27. Miranda-Moya, A.; Castañeda, H.; Wang, H. Fixed-Time Extended Observer-Based Adaptive Sliding Mode Control for a Quadrotor UAV under Severe Turbulent Wind. *Drones* 2023, 7, 700. [CrossRef]
- 28. Brescianini, D.; D'Andrea, R. An Omni-directional Multirotor Vehicle. Mechatronics 2018, 55, 76–93. [CrossRef]

Disclaimer/Publisher's Note: The statements, opinions and data contained in all publications are solely those of the individual author(s) and contributor(s) and not of MDPI and/or the editor(s). MDPI and/or the editor(s) disclaim responsibility for any injury to people or property resulting from any ideas, methods, instructions or products referred to in the content.